Clustering Point Process Based Network Topology Structure Constrained Urban Road Extraction From Remote Sensing Images

You Wu, Quanhua Zhao, Zhaoyu Shen, and Yu Li

***Abstract*—To extract complicated road network from remote sensing images on urban scenes, this article presents a clustering point process (CPP) based network topology structure constrained road extraction algorithm. Firstly, the CPP is constructed to model the feature points, such as endpoints, bends, and crossroads in a road system. Based on that, an initial network topology structure is constructed by connecting the points with lines. Then, according to the network structure characteristic and the spectral characteristic of road, a network topology structure constraining model and a spectral measurement constraining model are constructed, respectively. By combining the models above, a road extraction model is built under the framework of Bayes' theorem. Finally, to simulate from the road extraction model and extract an optimal road network, a solution strategy, reversible jump Markov Chain Monte Carlo (RJMCMC) simulation algorithm with related transfer operations, is designed according to the CPP and network topology structure. Several high-resolution remote sensing images on urban scenes are tested. According to a buffer evaluation method, and compared with the comparing algorithms, accuracy and extraction rate of results from the proposed algorithm are increased by 10.86% and 8.75% on average, respectively. It is proved that the proposed algorithm can extract the complicated road network effectively.**

***Index Terms*—Clustering point process (CPP), feature points, network topology structure, reversible jump Markov chain Monte Carlo (RJMCMC), urban road extraction.**

I. Introduction

ROAD is one of the most important infrastructures in urban systems. Therefore, it is of great significance to obtain urban road information timely and accurately in urban planning, traffic management, cartography, etc., [1]–[5]. All the time, remote sensing images are main data source for this purpose, while extracting urban road information from remote sensing images has always been an extremely difficult and challenging task, especially from ones with high spatial resolution. At present, scholars have proposed some sophisticated algorithms for road extraction. In terms of the level of characteristic utilization of road in images, the existing road extraction algorithms can be divided into algorithms of using spectral characteristic and algorithms of using both spectral and geometrical characteristics. The former algorithms, such as binarization [6], [7] and edge detection [8], [9] mainly rely on spectral information of pixels covered by roads in images, so they are easily interfered by geometric noises (e.g., cars and tree shadows). The latter algorithms, such as tracing algorithm [10]–[12] and least square algorithm [13], [14] are designed mainly by considering the local geometry (line with length and direction) of roads in images. They can avoid interference of geometric noises to some extent, but it is hard for them to extract the complete road networks if roads in images are crisscross. Interestingly, the point process (PP) based road extraction algorithm [15]–[17] is designed by combining the spectral, geometrical and network-structure characteristics of road, which has made many breakthroughs for extracting road accurately and completely. In the previous PP-based road extraction algorithms [18], [19], PP is used to model the location distribution of road, road segments are modeled by marking PP with local geometry of road, then a connected network model is constructed by constraining the relationships between road segments, and simultaneously a spectral measurement model of pixels covered by road segments is constructed according to the spectral characteristic of road. The previous algorithms can avoid interference of geometric noises greatly and extract the complete and connected road network, but their simulations are time-consuming and extraction results are not accurate enough especially at the crossroads. To improve the existing problems mentioned above, this article modifies the previous algorithms by changing modeling ways and focusing on the characteristics of location distribution and network structure of road.

The contributions of this article are as follows.

1) This article proposes that the endpoints, road bends, and crossroads in a road system can be considered as feature points showing the clustering characteristic along the road in a remote sensing image. Thus, the clustering point process (CPP) [20] is constructed to model the feature points.
2) Based on that, an initial network topology structure is constructed to characterize the network structure of road. Then, a road extraction model is constructed by constraining the network topology structure according

Manuscript received July 30, 2021; revised October 22, 2021; accepted February 12, 2022. Date of publication February 15, 2022; date of current version March 9, 2022. This work was supported in part by the Project for Key Scientific Issues from Education Department of Liaoning under Grant LJ2020ZD003, in part by the National Key Research and Development Program of China under Grant 2017YFB0504204, and in part by the Liaoning Revitalization Talents Program under Grant XLYC1802027. (*Corresponding author: Quanhua Zhao.*)

The authors are with the School of Geomatics, Liaoning Technical University, Fuxin 123000, China (e-mail: 1106193317@qq.com; zqhlby@163.com; 1904070613@stu.lntu.edu.cn; liyu@lntu.edu.cn).

Digital Object Identifier 10.1109/JSTARS.2022.3151757

This work is licensed under a Creative Commons Attribution 4.0 License. For more information, see https://creativecommons.org/licenses/by/4.0/

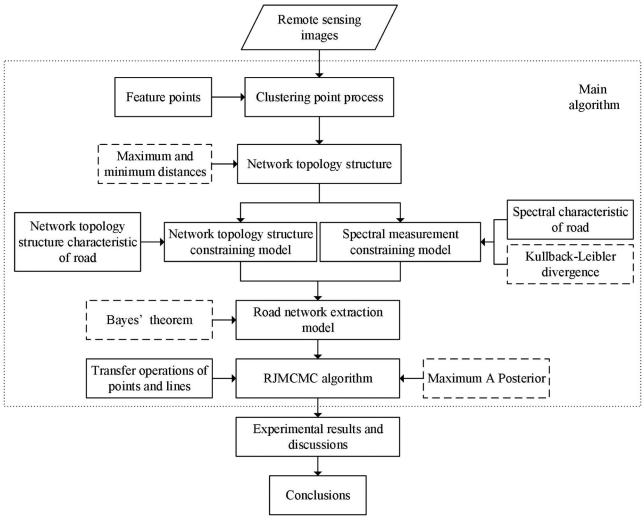

Fig. 1. Main flow of the proposed algorithm.

to the network-structure characteristic and the spectral characteristic of road.

3) Extremely related transfer operations of reversible jump Markov chain Monte Carlo (RJMCMC) simulation algorithm are designed to simulate from the road extraction model effectively.

To illustrate advantages of the proposed algorithm, high-resolution remote sensing images with complicated urban scenes are tested. The proposed algorithm is described in Section II. Section III shows experimental results from different road extraction algorithms and discussions on the extraction results. Finally, Section IV concludes this article.

II. Algorithm

Given a remote sensing image $\boldsymbol{z} = \{\boldsymbol{z}_i\,(x_i, y_i)\colon i = 1, \ldots, n\}$, where i is the index of pixels, n is the number of pixels, $(x_i, y_i) \in \boldsymbol{D}$ is the lattice coordinate of pixel i, $\boldsymbol{D}$ is the image domain (without confusion, $\boldsymbol{D}$ is used to denote the set of the lattice coordinates of all pixels), and $\boldsymbol{z}_i$ is the spectral measurement (vector) of pixel i. From the perspective of the spatial statistics, $\boldsymbol{z}$ can be regarded as the realization of random field $\boldsymbol{Z} = \{\boldsymbol{Z}_i\,(x_i, y_i)\colon i = 1, \ldots, n\}$ defined on $\boldsymbol{D}$, where $\boldsymbol{Z}_i$ is the random vector defined on the (x_i, y_i) and $\boldsymbol{z}_i$ is the realization of $\boldsymbol{Z}_i$.

A road system can be regarded as a continuous network topology structure of which the elements are road segments and road junctions, such as endpoints, bends, and crossroads. The junctions can be viewed as a set of feature points showing the clustering characteristic along the road. The real road network shows the network structure characteristic (e.g., connectivity and intersection). Besides, in the remote sensing image, the spectral homogeneity of pixels in road body and the spectral heterogeneity of pixels between road body and nonroad body around are obvious. As shown in in Fig. 1, the CPP model, network topology structure constraining model and spectral measurement constraining model can be constructed like the flowchart to accurately extract the complete road network.

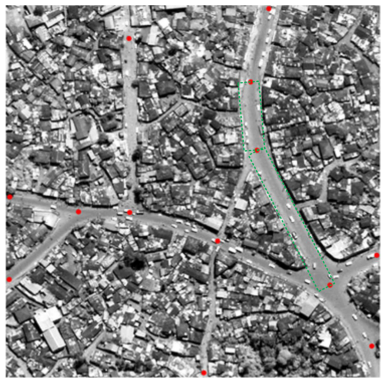

Fig. 2. 13 feature points of road network.

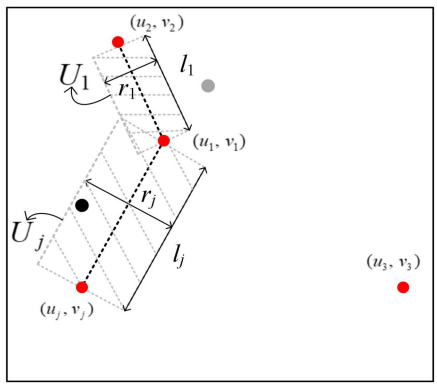

Fig. 3. Clustering region.

A. Clustering Point Process and Initial Network Topology Structure

As shown in Fig. 2, the feature points, such as the endpoints, bends, and crossroads represent the key locations of road network and show the clustering characteristic along the road. So, they can be viewed as a configuration of a CPP. First, let the set of feature points be $\boldsymbol{V} = \{(u_j, v_j)\colon j = 1, \ldots, m\}$, where j is the index of feature points, $(u_j, v_j) \in \boldsymbol{D}$ is the location coordinate of feature point j and m is the number of feature points. Assuming that the number m satisfies the Poisson distribution with mean β, where β is evaluated according to complexity and proportion of road in image

$$p(m) = \frac{\beta^m}{m!}\exp(-\beta). \tag{1}$$

Besides, as shown in Fig. 2, both the feature points and their related areas (see the green dotted rectangles) formed by the feature points are clustered in the road body. Therefore, to model the clustering characteristic of feature points, clustering regions are defined as the clustering measurement of CPP. As shown in Fig. 3, the clustering region U_j of (u_j, v_j) is constructed by the rectangle region with length $l_j = \min\{\|(u_j, v_j)-(u_1, v_1)\|_2, \ldots, \|(u_j, v_j)-(u_m, v_m)\|_2\}$ $(l_j \neq 0)$ and width $r_j = \omega_0 \ln(l_j)$, where $\|.\|_2$ is used to calculate the distance between two points, and ω_0 is a constant introduced to avoid the width too small or large.

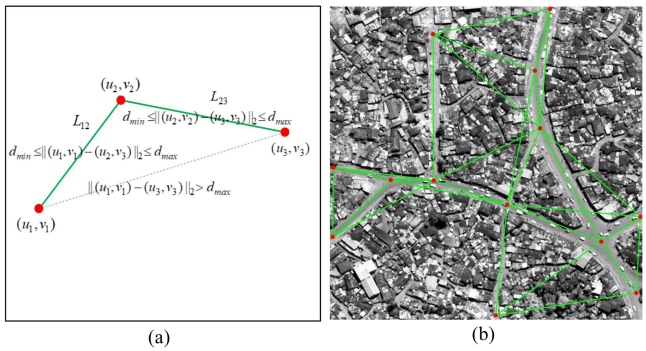

Fig. 4. Network topology structure. (a) Connection of three points. (b) An initial network

The probabilities of points falling into the clustering regions (or on the edge) should be larger than that of the other points to enhance the clustering characteristic, so probability density function (PDF) of the feature point can be given by

$$p((u_j, v_j)) = \begin{cases} \varsigma_1, \text{if } (u_j, v_j) \in \boldsymbol{U} \\ \varsigma_2, \text{if } (u_j, v_j) \notin \boldsymbol{U} \end{cases} \tag{2}$$

where ς_1 and ς_2 are constants closing to 1 and 0, respectively, and $\boldsymbol{U} = \{U_1 \cup U_2 \ \ldots \cup U_m\}$.

Based on the CPP, an initial network topology structure $\boldsymbol{L}$ can be generated by connecting the points in $\boldsymbol{V}$ with lines (which can be regarded as the road segments) according to the maximum and minimum distances. Let the maximum distance and minimum distance is $d_{\max}$ and $d_{\min}$, respectively. Given two points (u_j, v_j) and $(u_{j'}, v_{j'})$, if $d_{\min} \le \|(u_j, v_j) - (u_{j'}, v_{j'})\|_2 \le d_{\max}$, then they are connected, otherwise not connected. Therefore, an initial network topology structure is presented as $\boldsymbol{L} = \{L_{jj'}: d_{\min} \le \|(u_j, v_j) - (u_{j'}, v_{j'})\|_2 \le d_{\max}, j, j' = 1, \ldots, m, j \ne j'\}$, for example, in Fig. 4, the initial network topology structure is $\boldsymbol{L} = \{L_{12}, L_{23}\}$.

B. Network Topology Structure Constraining Model

Road system in an image shows network topology structure characteristics, such as the connectivity and intersection of network, thus, to ensure that $\boldsymbol{L}$ satisfies the characteristics, the freedom degree of point in $\boldsymbol{V}$ is defined and constrained, and included angles, distances between lines are calculated and constrained.

1) Constraining of Freedom Degree: To ensure that $\boldsymbol{L}$ is continuous at the bends, crossroads, etc., freedom degree ε of point is introduced and is defined as the number of lines connected by the point. As shown in Fig. 5, several local road structures, such as the road ends, straight roads, bending roads, road junctions with three, four, or more road segments are common in road system. Road ends can be represented by the points with $\varepsilon = 1$; straight roads and bending roads can be represented by the points with $\varepsilon = 2$; road junctions with three, four or more road segments can be represented by the points with $\varepsilon = 3, 4, \ldots$. These points with different freedom degrees can be constrained (punished or rewarded) by different energy values according to the complexity of whole road network.

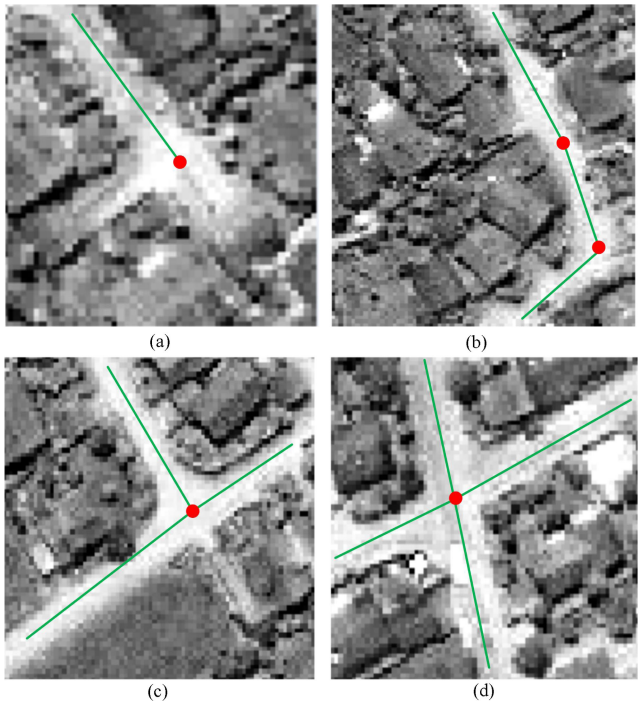

Fig. 5. Points with different freedom degrees. (a) Road end. (b) Straight and Bend roads. (c) Junctions with three road segments. (d) Junctions with four road segments.

In a road system, straight and bending roads are the most common structures in the whole road system, so the points with $\varepsilon = 2$ should account for the largest proportion and their energy values should be small. The proportions of road junctions with three and four road segments are smaller than the straight and bending roads, so energy values of the points with $\varepsilon = 3, 4$ are larger than the points with $\varepsilon = 2$. The proportion of road ends is usually determined by the test image and is larger than the road junctions, so energy values of the points with $\varepsilon = 1$ should be smaller than the points with $\varepsilon = 3, 4$. In this way, PDF of the freedom degree constraining is given by

$$p(\varepsilon_j) = \exp\left(-\begin{cases} \tau_0, \text{ if } \varepsilon_j = 0 \\ \tau_1, \text{ if } \varepsilon_j = 1 \\ \tau_2, \text{ if } \varepsilon_j = 2 \\ \tau_3, \text{ if } \varepsilon_j = 3 \\ \tau_4, \text{ if } \varepsilon_j = 4 \\ \tau_5, \text{ if } \varepsilon_j > 4 \end{cases}\right) \tag{3}$$

where ε_j represents the freedom degree of point j, and $\tau_0, \ldots, \tau_5$ are energy values which meet $\tau_2 < \tau_1 \le \tau_3 \le \tau_4 << \tau_0 << \tau_5$. If road junctions with five road segments appear in the testing image, $\tau_5 << \tau_0$ and new energy values will be introduced to constrain the points with $\varepsilon > 5$. The settings of energy values $\tau_0, \ldots, \tau_5$ are given in Section III.

2) Constraining of Included Angles and Distances: To avoid sharp angles appearing in $\boldsymbol{L}$, included angles and distances between lines are calculated and constrained. Given two lines L and L' in $\boldsymbol{L}$, suppose that their directions are θ_L and $\theta_{L'}$, lengths are l_L and $l_{L'}$, and coordinates of midpoints are (u_L, v_L) and

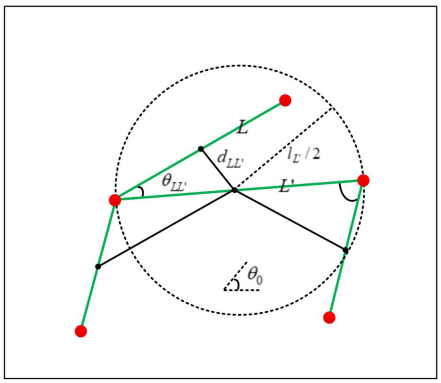

Fig. 6. Included angles and distances between lines. Black points are midpoints of lines.

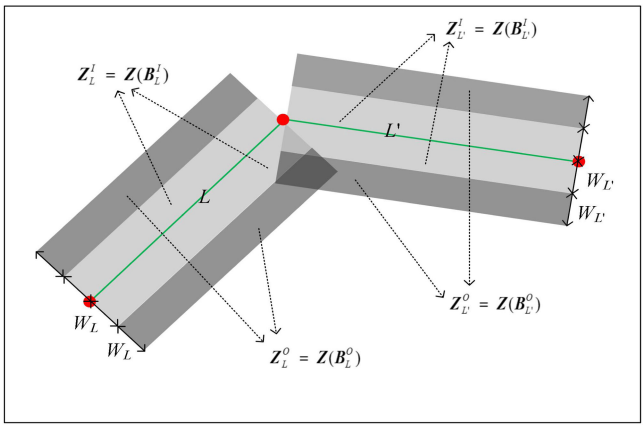

Fig. 7. Modeling of road body and nonroad body.

$(u_{L'}, v_{L'})$, respectively. Then their included angle and distance can be calculated by $\theta_{LL'} = \min\{|\theta_L - \theta_{L'}|, \pi - |\theta_L - \theta_{L'}|\}$ and $d_{LL'} = \|(u_L, v_L) - (u_{L'}, v_{L'})\|_2$, respectively. If $\theta_{LL'} < \theta_0$ (a small angle threshold) and $d_{LL'} \le \max\{l_L, l_{L'}\}/2$, the two lines are adjacent and their included angle is sharp (see L and L' in Fig. 6), so this state should be punished by a large energy value. If $\theta_{LL'} \ge \theta_0$ or $d_{LL'} > \max\{l_L, l_{L'}\}/2$, this state is accepted (see Fig. 6), so its energy is 0. In this way, PDF of included angles and distances constraining can be given by

$$p(\theta_{LL'}, d_{LL'}) = \exp\left(-\begin{cases}\tau_6, & \text{if } d_{LL'} \le \frac{\max\{l_L, l_{L'}\}}{2} \wedge \theta_{LL'} < \theta_0 \\ 0, & \text{if } \neg(d_{LL'} \le \frac{\max\{l_L, l_{L'}\}}{2} \wedge \theta_{LL'} < \theta_0)\end{cases}\right) \tag{4}$$

where τ_6 is a large energy to stop lines forming sharp angles, "$\wedge$" and "$\neg$" represent AND and NO operators, respectively.

C. Spectral Measurement Constraining Model

In a remote sensing image, road has the spectral homogeneity in road body and the spectral heterogeneity between road body and nonroad body around. Thus, to constrain the spectral measurement of $\boldsymbol{L}$, road body and nonroad body belonging to $\boldsymbol{L}$ are required to be modeled. As shown in Fig. 7, for any line L in $\boldsymbol{L}$, its road body (light gray region) and nonroad body (dark gray region) are modeled by rectangles with width W_L. They are distributed at both sides of L with distances 0 and W_L. W_L is a variable taking in a width interval evaluated according to the average width of road surface. Since the coordinates of pixels covered by L are known, the coordinates of pixels covered by road body and nonroad body can be calculated. For any line L in $\boldsymbol{L}$, let $\boldsymbol{B}_L^I$ and $\boldsymbol{B}_L^O$ be coordinate sets of pixels covered by the road body and nonroad body, respectively. Then, given an image $\boldsymbol{Z} = \{\boldsymbol{Z}_i\,(x_i, y_i)\colon i = 1, \ldots, n\}$, the spectral values of pixels covered by road body and nonroad body can be calculated according to the mapping from coordinates of pixels to spectral values of pixels. In this way, the spectral values $\boldsymbol{Z}_L^I$ and $\boldsymbol{Z}_L^O$ of pixels covered by road body and nonroad body belonging to L can be calculated by the mappings $\boldsymbol{Z}_L^I = \boldsymbol{Z}(\boldsymbol{B}_L^I)$ and $\boldsymbol{Z}_L^O = \boldsymbol{Z}(\boldsymbol{B}_L^O)$, respectively.

To measure the homogeneity of spectral values of pixels covered by road body belonging to L, suppose that every spectral value in $\boldsymbol{Z}_L^I$ satisfies independent and identical Gaussian distribution

$$\begin{aligned} p(\boldsymbol{Z}_L^I|L) &= \prod_{Z_L^I \in \boldsymbol{Z}_L^I} p(Z_L^I|L) \\ &= \prod_{Z_L^I \in \boldsymbol{Z}_L^I} \frac{1}{\sqrt{2\pi}\sigma^I} \exp\left(-\frac{(Z_L^I - \mu^I)^2}{2(\sigma^I)^2}\right) \end{aligned} \tag{5}$$

where μ^I and σ^I are mean and standard deviation of spectral values of pixels covered by the road body, respectively. Similarly, suppose that every spectral value in $\boldsymbol{Z}_L^O$ satisfies independent and identical Gaussian distribution

$$\begin{aligned} p(\boldsymbol{Z}_L^O|L) &= \prod_{Z_L^O \in \boldsymbol{Z}_L^O} p(Z_L^O|L) \\ &= \prod_{Z_L^O \in \boldsymbol{Z}_L^O} \frac{1}{\sqrt{2\pi}\sigma^O} \exp\left(-\frac{(Z_L^O - \mu^O)^2}{2(\sigma^O)^2}\right) \end{aligned} \tag{6}$$

where μ^O and σ^O are mean and standard deviation of spectral values of pixels covered by the nonroad body, respectively. To measure the heterogeneity of spectral values in $\boldsymbol{Z}_L^I$ and $\boldsymbol{Z}_L^O$, Kullback–Leibler (K–L) divergence [21], [22], which is an effective measurement to characterize the difference between two probability distributions, is used. Its negative value can be used to define energy function of the heterogeneity. Therefore, the symmetric form of K–L divergence is used to calculate energy function of heterogeneity between $p(\boldsymbol{Z}_L^I|L)$ and $p(\boldsymbol{Z}_L^O|L)$

$$\begin{aligned} E(\boldsymbol{Z}_L^I, \boldsymbol{Z}_L^O) = &-p(\boldsymbol{Z}_L^I|L)\log\frac{p(\boldsymbol{Z}_L^I|L)}{p(\boldsymbol{Z}_L^O|L)} \\ &-p(\boldsymbol{Z}_L^O|L)\log\frac{p(\boldsymbol{Z}_L^O|L)}{p(\boldsymbol{Z}_L^I|L)}. \end{aligned} \tag{7}$$

Its PDF is expressed as $p(\boldsymbol{Z}_L^I, \boldsymbol{Z}_L^O|\,L) = \exp(-E(\boldsymbol{Z}_L^I, \boldsymbol{Z}_L^O))$. For all lines in $\boldsymbol{L}$, it is assumed that their PDFs of the homogeneity and heterogeneity are independent of each other. Therefore, the spectral measurement constraining model of $\boldsymbol{L}$ is given by (9)

$$p(\boldsymbol{Z}|\boldsymbol{L}) \propto p\left(\boldsymbol{Z}_{\boldsymbol{L}}^{I}|\boldsymbol{L}\right) p\left(\boldsymbol{Z}_{\boldsymbol{L}}^{O}|\boldsymbol{L}\right) p\left(\boldsymbol{Z}_{L}^{I}, \boldsymbol{Z}_{L}^{O}|\boldsymbol{L}\right) = \prod_{L\in\boldsymbol{L}} p\left(\boldsymbol{Z}_{L}^{I}|L\right) \prod_{L\in\boldsymbol{L}} p\left(\boldsymbol{Z}_{L}^{O}|L\right) \prod_{L\in\boldsymbol{L}} p\left(\boldsymbol{Z}_{L}^{I}, \boldsymbol{Z}_{L}^{O}|L\right). \tag{8}$$

D. Road Extraction Model

To sum up, $\boldsymbol{V}$ and m are built to characterize the clustering characteristic of road, $\boldsymbol{L}$ is built to characterize the network topology structure of road. Therefore, given an image $\boldsymbol{Z}$, and under the framework of Bayes' theorem [23]–[26], the *posterior* PDF for road extraction is given as in (9). The parameter set $\{\boldsymbol{V}, m, \boldsymbol{L}\}$ can characterize a configuration which can be simulated by RJMCMC algorithm effectively. The optimal results can be obtained according to the maximum *a posterior* [27], [28] criterion

$$\begin{aligned} p(\boldsymbol{V}, m, \boldsymbol{L}|\mathbf{Z}) &\propto p(\boldsymbol{V}, m, \boldsymbol{L}, \mathbf{Z}) = p(\mathbf{Z}|\boldsymbol{V}, m, \boldsymbol{L}) p(\boldsymbol{V}, m, \boldsymbol{L}) \\ &= p(\mathbf{Z}|\boldsymbol{L}) p(\boldsymbol{L}|\boldsymbol{V}, m) p(\boldsymbol{V}|m) p(m) \\ &= \prod_{L\in\boldsymbol{L}} p\left(\boldsymbol{Z}_{L}^{I}|L\right) \prod_{L\in\boldsymbol{L}} p\left(\boldsymbol{Z}_{L}^{O}|L\right) \prod_{L\in\boldsymbol{L}} p\left(\boldsymbol{Z}_{L}^{I}, \boldsymbol{Z}_{L}^{O}|L\right) \prod_{j=1}^{m} p(\varepsilon_j) \\ &\quad \prod_{L,L'\in\boldsymbol{L}, L\neq L'} p\left(\theta_{LL'}, d_{LL'}\right) \prod_{j=1}^{m} p((u_j, v_j)) \frac{\beta^m}{m!} \exp(-\beta). \end{aligned} \tag{9}$$

E. RJMCMC Simulation Algorithm

It can be seen from the road extraction model that extraction process of optimal road is actually a solution process of parameter set $\boldsymbol{S} = \{\boldsymbol{V}, m, \boldsymbol{L}\}$. When m changes, the corresponding dimensions of vectors $\boldsymbol{V}$ and $\boldsymbol{L}$ also change. RJMCMC algorithm [29]–[31] is an effective method which can perform reversible jumps between configurations with different dimensions. The configurations are characterized by parameter sets at different iterations. The jumps are proposed according to transfer operations designed in advance to update the configurations (parameter sets). The basic idea of RJMCMC algorithm is to calculate acceptance rate of the jumping from a configuration to another configuration. At $(t+1)$th iteration, suppose that the current configuration characterized by parameter set is $\boldsymbol{S}^{(t)} = (\boldsymbol{V}^{(t)}, \boldsymbol{L}^{(t)}, m^{(t)})$ and the candidate configuration proposed by transfer operations can be given by $\boldsymbol{S}^{*} = (\boldsymbol{S}^{(t)}, \varphi)$, where φ is a continuous random vector which is defined to ensure the dimension balance between $\boldsymbol{S}^{*}$ and $\boldsymbol{S}^{(t)}$, i.e., $dim(\boldsymbol{S}^{*}) = dim(\boldsymbol{S}^{(t)}) \pm dim(\varphi)$, where $dim(.)$ is a function that calculates the dimension of vector. The acceptance rate of jumping proposed by one transfer operation is calculated by

$$\alpha\left(\boldsymbol{S}^{(t)}, \boldsymbol{S}^{*}\right) = \min\left\{1, \frac{p\left(\boldsymbol{Z}\left|\boldsymbol{S}^{*}\right.\right) p\left(\boldsymbol{S}^{*}\right) q\left(\boldsymbol{S}^{*}\right)}{p\left(\boldsymbol{Z}\left|\boldsymbol{S}^{(t)}\right.\right) p\left(\boldsymbol{S}^{(t)}\right) q\left(\boldsymbol{S}^{(t)}\right) p(\varphi)} \left|\frac{\partial\left(\boldsymbol{S}^{*}\right)}{\partial\left(\boldsymbol{S}^{(t)}, \varphi\right)}\right|\right\} \tag{10}$$

where $p(\varphi)$ is the PDF of random vector φ, $q(\boldsymbol{S}^{(t)})$ is PDF of transfer operation from $\boldsymbol{S}^{(t)}$ to $\boldsymbol{S}^{*}$, $q(\boldsymbol{S}^{*})$ is PDF of the reverse transfer operation from $\boldsymbol{S}^{*}$ to $\boldsymbol{S}^{(t)}$, and $|\partial(\boldsymbol{S}^{*}) / \partial(\boldsymbol{S}^{(t)}, \varphi)|$ is the Jacobian [32], [33]. If $\alpha \geq$ num (a random number uniformly distributed in [0, 1]), the candidate configuration is accepted, i.e., $\boldsymbol{S}^{(t+1)} = (\boldsymbol{S}^{(t)}, \varphi)$, otherwise rejected, i.e., $\boldsymbol{S}^{(t+1)} = \boldsymbol{S}^{(t)}$. Noting that if $I\text{^}t$ is lower than it, where $I \in [0.99, 0.9999]$ and it is a threshold set according to complexity and sizes of road scenes and $0 < it < 1$), the result obtained is considered to be optimal. Obviously, designing related transfer operations is key to obtaining the optimal road effectively. This article designs the operations birth, death and move of point for changing $\boldsymbol{V}^{(t)}$ and birth, death and transformations of line for changing $\boldsymbol{L}^{(t)}$.

1) Birth, Death and Move of Point: To ensure that new generated points can improve the quality of the current network, new related points can be generated based on the CPP. Randomly selecting a point $(u_j^{(t)}, v_j^{(t)})$ in $\boldsymbol{V}^{(t)}$, a new point can be generated in clustering region $U_j^{(t)}$. Taking Fig. 8(a) as an example, the point $(u_1^{(t)}, v_1^{(t)})$ is selected randomly, its clustering region $U_1^{(t)}$ with length $l_1^{(t)} = \|(u_1^{(t)}, v_1^{(t)}) - (u_2^{(t)}, v_2^{(t)})\|_2$ and width $r_1^{(t)} = \omega_0 \ln(l_1^{(t)})$ can be obtained, then a new point (u_*, v_*) can be generated in $U_1^{(t)}$. Then, for each point $(u_j^{(t)}, v_j^{(t)})$ $(j = 1, \ldots, m^{(t)})$ in $\boldsymbol{V}^{(t)}$, if distance between points (u_*, v_*) and $(u_j^{(t)}, v_j^{(t)})$ satisfies $d_{\min} \leq \|(u_j, v_j) - (u_*, v_*)\|_2 \leq d_{\max}$, line L_{j*} will be generated correspondingly [e.g., the new lines L_{1*} and L_{2*} in Fig. 8(b)]; otherwise will not be generated.

In this way, suppose that $\boldsymbol{S}^{*} = \{\boldsymbol{V}^{*}, m^{(t)}+1, \boldsymbol{L}^{*}\}$, the corresponding acceptance rate is calculated as. (11) shown at the bottom of this page, where N_o is the number of points in the clustering region of the point selected randomly, $q_{\boldsymbol{V}b}(\boldsymbol{S}^{(t)})$ is PDF of birth transfer operation of point, $q_{\boldsymbol{V}d}(\boldsymbol{S}^{*})$ is PDF of death transfer operation of point. If $\alpha_{\boldsymbol{V}b}(\boldsymbol{S}^{(t)}, \boldsymbol{S}^{*}) \geq$ num, the (u_*, v_*) will be accepted; otherwise will be rejected. Similarly, the death operation is designed based on the CPP. Randomly selecting a point $(u_j^{(t)}, v_j^{(t)})$ in $\boldsymbol{V}^{(t)}$, a point in clustering region $U_j^{(t)}$ can be deleted randomly. The corresponding acceptance rate can be simply represented by $\alpha_{\boldsymbol{V}d}(\boldsymbol{S}^{(t)}, \boldsymbol{S}^{*}) = \alpha_{\boldsymbol{V}b}{}^{-1}(\boldsymbol{S}^{*}, \boldsymbol{S}^{(t)})$.

The move operation of point is easier than the birth and dearth operations. Randomly selecting a point $(u_j^{(t)}, v_j^{(t)})$ in $\boldsymbol{V}^{(t)}$, a point in clustering region $U_j^{(t)}$ can be moved randomly. Taking Fig. 9 as an example, if point $(u_1^{(t)}, v_1^{(t)})$ is selected randomly,

$$\begin{aligned} \alpha_{\boldsymbol{V}b}\left(\boldsymbol{S}^{(t)}, \boldsymbol{S}^{*}\right) &= \min\left\{1, \frac{p\left(\boldsymbol{Z}\left|\boldsymbol{S}^{*}\right.\right) p\left(\boldsymbol{S}^{*}\right) q_{\boldsymbol{V}d}\left(\boldsymbol{S}^{*}\right)}{p\left(\boldsymbol{Z}\left|\boldsymbol{S}^{(t)}\right.\right) p\left(\boldsymbol{S}^{(t)}\right) q_{\boldsymbol{V}b}\left(\boldsymbol{S}^{(t)}\right) p(\varphi)} \left|\frac{\partial\left(\boldsymbol{S}^{*}\right)}{\partial\left(\boldsymbol{S}^{*}, \varphi\right)}\right|\right\} \\ &= \min\left\{1, \frac{\beta}{(m^{(t)}+1)} \frac{p(\boldsymbol{V}^{*}\left|m^{(t)}+1\right.) p(\boldsymbol{L}^{*}\left|\boldsymbol{V}^{*}, m^{(t)}+1\right.) p(\boldsymbol{Z}\left|\boldsymbol{L}^{*}\right.) q_{\boldsymbol{V}d}(\boldsymbol{S}^{*})}{N_o p(\boldsymbol{V}^{(t)}|m^{(t)}) p(\boldsymbol{L}^{(t)}|\boldsymbol{V}^{(t)}, m^{(t)}) p(\boldsymbol{Z}\left|\boldsymbol{L}^{(t)}\right.) q_{\boldsymbol{V}b}(\boldsymbol{S}^{(t)}) p(\varphi)} \left|\frac{\partial\left(\boldsymbol{S}^{*}\right)}{\partial\left(\boldsymbol{S}^{(t)}, \varphi\right)}\right|\right\} \end{aligned} \tag{11}$$

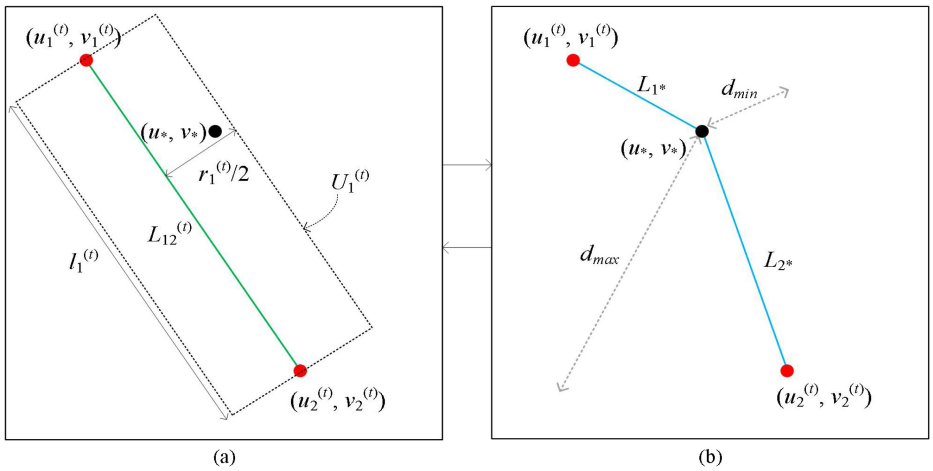

Fig. 8. Birth operation for changing $\boldsymbol{V}^{(t)}$. (a) New point (black) generated in the clustering region. (b) New lines generated according to $d_{\min} \leq \|(u_j, v_j) - (u_*, v_*)\|_2 \leq d_{\max}, j = 1, 2$.

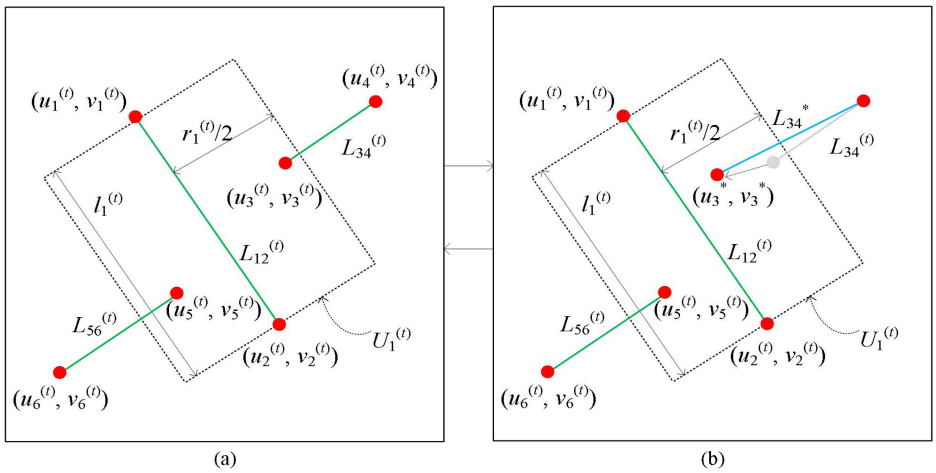

Fig. 9. Move operation for changing $\boldsymbol{V}^{(t)}$. (a) Point selection. (b) Move of the point.

point $(u_3^{(t)}, v_3^{(t)})$ randomly selected in clustering region $U_1^{(t)}$ is moved. In this way, the dimension of new configuration is not changed, the corresponding acceptance rate is calculated as (12) shown at the bottom of the next page, where $q_{\boldsymbol{V}m}(\boldsymbol{S}^{(t)})$ is PDF of move transfer operation of point, $q_{\boldsymbol{V}m*}(\boldsymbol{S}^*)$ is PDF of reverse transfer operation of move.

2). Birth, Death and Transformations of Line: To obtain a connected $\boldsymbol{L}$, the operations for changing $\boldsymbol{L}^{(t)}$ are designed. Randomly selecting a point $(u_j^{(t)}, v_j^{(t)})$ in $\boldsymbol{V}^{(t)}$ and given a circle with radius d (a threshold), if one or more points fall into the circle, then the point $(u_{j'}^{(t)}, v_{j'}^{(t)})$ closest to $(u_j^{(t)}, v_j^{(t)})$ is connected with $(u_j^{(t)}, v_j^{(t)})$ by a new generated line $L_{jj'}{}^*$; otherwise a new line L^* is generated with length $l^* = d$ and direction θ^* is uniformly selected in $[\theta_j\text{-}\pi/Q, \theta_j{+}\pi/Q]$, where π/Q is a small angle. Taking Fig. 10 as an example, point $(u_4^{(t)}, v_4^{(t)})$ in $\boldsymbol{V}^{(t)}$ is selected and circle is given, a point $(u_2^{(t)}, v_2^{(t)})$ falls into the circle, then $(u_4^{(t)}, v_4^{(t)})$ and $(u_2^{(t)}, v_2^{(t)})$ are connected by a new line $L_{24}{}^*$ [see Fig. 10(b)]; but, if no point falls into the circle [see Fig. 10(c)], a new line L^* with a endpoint (u^*, v^*) is generated.

In this way, suppose that $\boldsymbol{S}^* = \{\boldsymbol{V}^*, m^*, \boldsymbol{L}^*\}$, the corresponding acceptance rate is calculated by (13) shown at the bottom of this

$$\begin{aligned}\alpha_{\boldsymbol{V}m}\left(\boldsymbol{S}^{(t)}, \boldsymbol{S}^*\right) &= \min\left\{1, \frac{p\left(\boldsymbol{Z}\left|\boldsymbol{S}^*\right.\right) p\left(\boldsymbol{S}^*\right) q_{\boldsymbol{V}m*}\left(\boldsymbol{S}^*\right)}{p\left(\boldsymbol{Z}\left|\boldsymbol{S}^{(t)}\right.\right) p\left(\boldsymbol{S}^{(t)}\right) q_{\boldsymbol{V}m}\left(\boldsymbol{S}^{(t)}\right)}\right\} \\ &= \min\left\{1, \frac{p(\boldsymbol{V}^*\left|m^{(t)}\right.)p(\boldsymbol{L}^*\left|\boldsymbol{V}^*, m^{(t)}\right.)p(\boldsymbol{Z}\left|\boldsymbol{L}^*\right.)q_{\boldsymbol{V}m*}(\boldsymbol{S}^*)}{N_o p(\boldsymbol{V}^{(t)}|m^{(t)})p(\boldsymbol{L}^{(t)}|\boldsymbol{V}^{(t)}, m^{(t)})p(\boldsymbol{Z}\left|\boldsymbol{L}^{(t)}\right.)q_{\boldsymbol{V}m}(\boldsymbol{S}^{(t)})}\right\}\end{aligned} \tag{12}$$

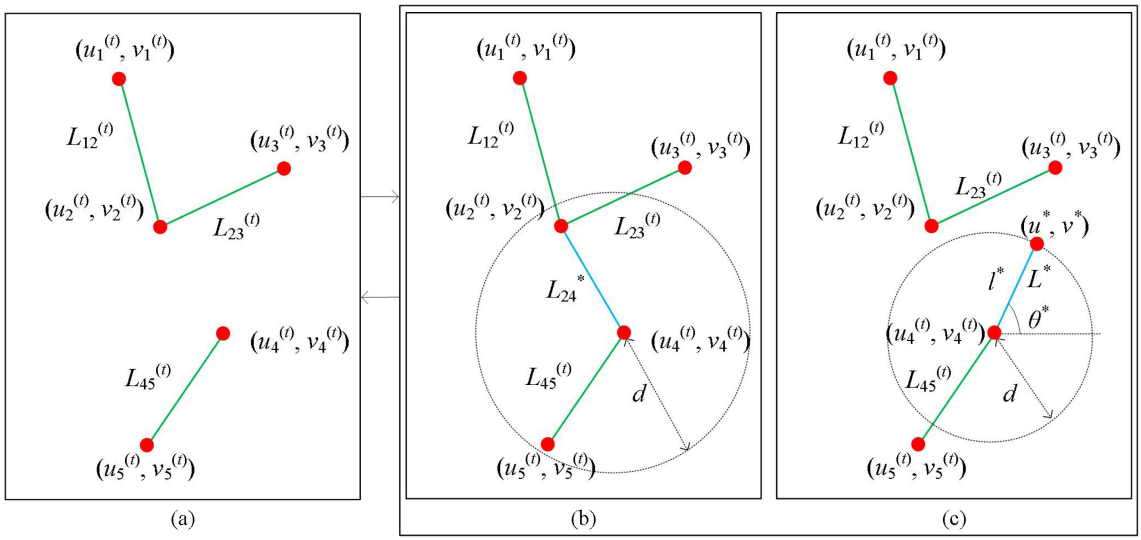

Fig. 10. Birth operation of line for changing $L^{(t)}$. (a) Selection of a point. (b) (c) Birth of a new line.

page, where N_b is the number of points within the range of distance d, $q_{\boldsymbol{L}b}(\boldsymbol{S}^{(t)})$ is PDF of birth transfer operation of line, $q_{\boldsymbol{L}d}(\boldsymbol{S}^{*})$ is PDF of death transfer operation of line. If $\alpha_{\boldsymbol{L}b}(\boldsymbol{S}^{(t)}, \boldsymbol{S}^{*}) \geq num$, new line is accepted; otherwise rejected. Similarly, the death operation is designed as the same way. Randomly selecting a point $(u_j^{(t)}, v_j^{(t)})$ in $\boldsymbol{V}^{(t)}$, another point within the range of distance d can be deleted randomly. The corresponding acceptance rate can be simply represented by $\alpha_{\boldsymbol{L}d}(\boldsymbol{S}^{(t)}, \boldsymbol{S}^{*}) = \alpha_{\boldsymbol{L}b}{}^{-1}(\boldsymbol{S}^{*}, \boldsymbol{S}^{(t)})$.

The transformations of line are designed by changing position (mobile), length (elastic) and direction (rotary). Randomly selecting a line $L_{jj'}$ in $\boldsymbol{L}^{(t)}$, then its position, length and direction can be transformed with transformation variables $(\Delta x, \Delta y)$, Δl and $\Delta\theta$, respectively. Noting that its related points $(u_j^{(t)}, v_j^{(t)})$, $(u_{j'}^{(t)}, v_{j'}^{(t)})$ and lines connected by $(u_j^{(t)}, v_j^{(t)})$, $(u_{j'}^{(t)}, v_{j'}^{(t)})$ will also be changed correspondingly. Taking Fig. 11 as an example, line $L_{23}{}^{(t)}$ is transformed to $L_{23}{}^{*}$ according to position, length and direction transformations, then the related end points $(u_2^{(t)}, v_2^{(t)})$, $(u_3^{(t)}, v_3^{(t)})$ and lines $L_{12}{}^{(t)}$, $L_{34}{}^{(t)}$ are also changed to $(u_2{}^{*}, v_2{}^{*})$, $(u_3{}^{*}, v_3{}^{*})$ and lines $L_{12}{}^{*}, L_{34}{}^{*}$. The dimension of new configuration is not changed, their corresponding acceptance rates can be calculated as (14) shown at the bottom of this page, where $q_{\boldsymbol{L}T}(\boldsymbol{S}^{(t)})$ represents PDF of any transformation transfer operation of line, $q_{\boldsymbol{L}T*}(\boldsymbol{S}^{*})$ is PDF of reverse transfer operation of the transformation.

III. Experimental Results and Discussions

A. Datasets, Parameter Setting, and Buffer Evaluation Method

Datasets are given in Table I. All images cover urban scenes with different road network structure characteristic and spectral characteristic, where WorldView-1 satellite image is with 0.4 m resolution and covers the urban road scene in Addis Ababa, Ethiopia; Google Earth image is with about 1 m resolution and covers the urban road scene in the west area of Beijing, China; Gaofen-2 satellite image is with 0.8 m resolution and covers the urban road scene in Shenyang, China; Ikonos satellite image is with 1 m resolution and covers the urban road scene in Deutsches

$$\begin{aligned}\alpha_{\boldsymbol{L}b}\left(\boldsymbol{S}^{(t)}, \boldsymbol{S}^{*}\right) &= \min\left\{1, \frac{p\left(\boldsymbol{Z}\left|\boldsymbol{S}^{*}\right.\right) p\left(\boldsymbol{S}^{*}\right) q_{\boldsymbol{L}d}\left(\boldsymbol{S}^{*}\right)}{p\left(\boldsymbol{Z}\left|\boldsymbol{S}^{(t)}\right.\right) p\left(\boldsymbol{S}^{(t)}\right) q_{\boldsymbol{L}b}\left(\boldsymbol{S}^{(t)}\right) p\left(\phi\right)} \left|\frac{\partial\left(\boldsymbol{S}^{*}\right)}{\partial\left(\boldsymbol{S}^{*}, \phi\right)}\right|\right\} \\ &= \left\{\min\left\{1, \frac{N_b p(\boldsymbol{L}^{*}\left|\boldsymbol{V}^{*}, m^{*}\right.) p(\boldsymbol{Z}|\boldsymbol{L}^{*}) q_{\boldsymbol{L}d}(\boldsymbol{S}^{*})}{p(\boldsymbol{L}^{(t)}|\boldsymbol{V}^{(t)}, m^{(t)}) p(\boldsymbol{Z}|\boldsymbol{L}^{(t)}) q_{\boldsymbol{L}b}(\boldsymbol{S}^{(t)}) p(\phi)} \left|\frac{\partial\left(\boldsymbol{S}^{*}\right)}{\partial\left(\boldsymbol{S}^{(t)}, \phi\right)}\right|\right\}\right.\end{aligned} \tag{13}$$

$$\begin{aligned}\alpha_{\boldsymbol{L}T}\left(\boldsymbol{S}^{(t)}, \boldsymbol{S}^{*}\right) &= \min\left\{1, \frac{p\left(\boldsymbol{Z}\left|\boldsymbol{S}^{*}\right.\right) p\left(\boldsymbol{S}^{*}\right) q_{\boldsymbol{L}T*}\left(\boldsymbol{S}^{*}\right)}{p\left(\boldsymbol{Z}\left|\boldsymbol{S}^{(t)}\right.\right) p\left(\boldsymbol{S}^{(t)}\right) q_{\boldsymbol{L}T}\left(\boldsymbol{S}^{(t)}\right)}\right\} \\ &= \min\left\{1, \frac{p(\boldsymbol{V}^{*}\left|m^{(t)}\right.) p(\boldsymbol{L}^{*}\left|\boldsymbol{V}^{*}, m^{(t)}\right.) p(\boldsymbol{Z}\left|\boldsymbol{L}^{*}\right.) q_{\boldsymbol{L}T*}(\boldsymbol{S}^{*})}{p(\boldsymbol{V}^{(t)}|m^{(t)}) p(\boldsymbol{L}^{(t)}|\boldsymbol{V}^{(t)}, m^{(t)}) p(\boldsymbol{Z}\left|\boldsymbol{L}^{(t)}\right.) q_{\boldsymbol{L}T}(\boldsymbol{S}^{(t)})}\right\}\end{aligned} \tag{14}$$

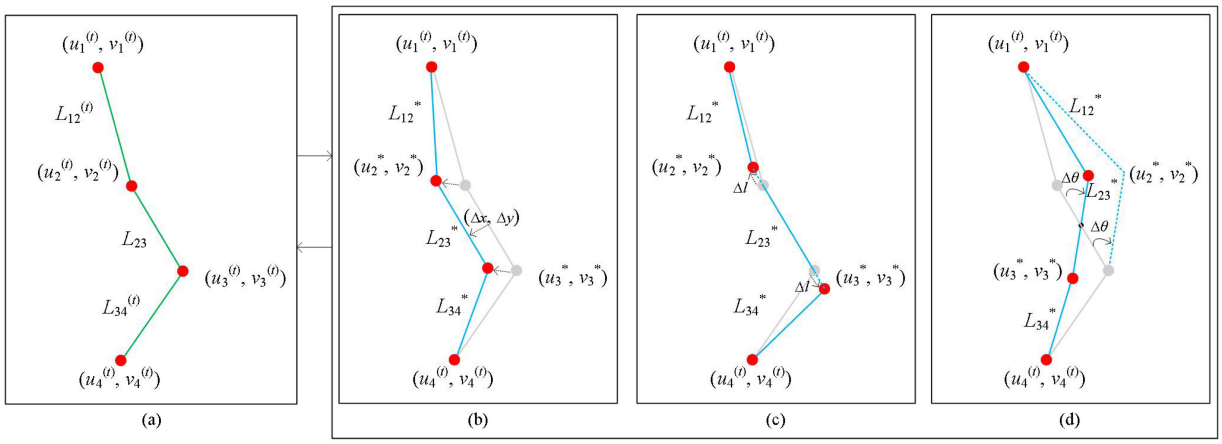

Fig. 11. Transformations of line for changing $\boldsymbol{L}^{(t)}$. (a) Selection of a line. (b) Position transformation in any direction. (c) Length transformation at one end or both ends of the line. (d) Direction transformation at midpoint or one end of the line.

TABLE I
OVERVIEW OF THE DATASETS AND INITIAL PARAMETER

Dataset	Resolution (metre)	Size (pixels)	Initial parameter
WorldView-1	0.4	1151 × 1257	26 feature points, 91 lines, $d_{min} = 40$, $d_{max} = 200$
Google Earth Image	≈ 1	2494 × 2303	26 feature points, 134 lines, $d_{min} = 80$, $d_{max} = 400$
Gaofen-2	0.8	2144 × 2226	27 feature points, 280 lines, $d_{min} = 60$, $d_{max} = 350$
Ikonos	1	700 × 700	30 feature points, 312 lines, $d_{min} = 20$, $d_{max} = 120$
		400 × 400	25 feature points, 96 lines, $d_{min} = 10$, $d_{max} = 80$
QuickBird	0.61	1024 × 1024	25 feature points, 75 lines, $d_{min} = 20$, $d_{max} = 150$

TABLE II
HYPERPARAMETER SETTING RULE

Parameters	Setting rule
β	It is set according to the distribution, curvature and proportion of road network in an image.
ω_0	$\omega_0 \in [2, 10]$ which is obtained according to the width of road surface and resolution of image.
τ_0	$\tau_0 \approx a_0 \times 1/0.9999\text{^}t$, where a_0 is a constant and t is the number of iterations.
τ_1, τ_2, τ_3, τ_4, τ_5	$\tau_1 \approx \tau_0$ - 0.13; $\tau_2 \approx a_1 \times 0.9999\text{^}t + 0.13$ (a_1 is a constant); $\tau_3 \approx 2a_1 \times 0.9999\text{^}t + 0.13$; $\tau_4 \approx 2a_1 \times 0.9999\text{^}t + 0.26$; $\tau_5 \approx \tau_0 + 0.13$
τ_6	It is a large value defined to stop the adjacent lines tending to overlap and $\tau_6 > \tau_5$.
θ_0	$\theta_0 \in (0°, 30°)$ which is set according to curvature of road network.
W	It is set according to the width of road surface and resolution of image.
d_{min}, d_{max}, d	d_{min} and d_{max} are set according to the size of image. d is set according to the curvature of road and resolution of image.
$(\Delta x, \Delta y)$, Δl, $\Delta\theta$	They are set according to the resolution of image and curvature of road.

Zentrum für Luft-und Raumfahrt zone, German; and QuickBird satellite image is with 0.61 m resolution and covers the urban road scene with many large tree shadows. Besides, Table I gives the sizes of testing images and initial state of each experiment.

In the proposed algorithm, main hyperparameters which are evaluated according to the experimental experience and information of datasets. Table II gives the setting rule of all hyperparameters in the proposed algorithm.

Besides, to evaluate experimental results quantitatively, the buffer evaluation method [34] is modeled. The buffer region is obtained by buffering the standard road network (reference line). Fig. 12(a) gives an example of buffer model with three layers, the red grids are pixels covered by reference line, the yellow, blue and green grids are first layer, second layer and third layer of buffer region, respectively. Obviously, the reference is 0th layer of buffer region. Let $\boldsymbol{K}_e$, $e = 0, 1, 2, 3, \ldots, h$, be the set of pixels covered by eth layer of buffer, where e and h are index and total number of buffer layers, respectively, and $\boldsymbol{K}_E$ be the set of pixels covered by the extracted road network. As shown in (15) and (16), the percentages between the number of pixels in different buffers and the total number of pixels in $\boldsymbol{K}_E$ are calculated to evaluate the accuracy and extraction rate

$$k_e = \frac{\phi\{(x,y) : (x,y) \in \boldsymbol{K}_e \cap \boldsymbol{K}_E\}}{\phi\{(x,y) : (x,y) \in \boldsymbol{K}_E\}} \tag{15}$$

$$K_h = \sum_{e=0}^{h} k_e \tag{16}$$

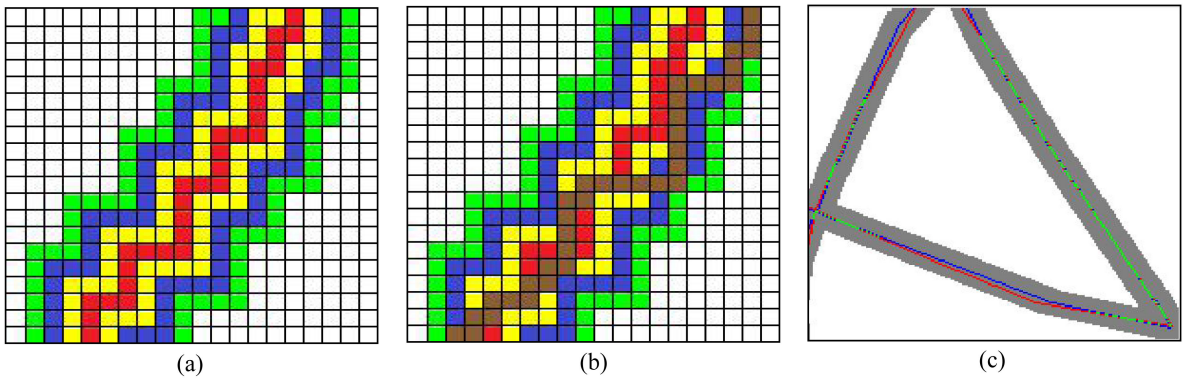

Fig. 12. Buffer model. (a) and (b) $\boldsymbol{K}_0$ = red pixels, $\boldsymbol{K}_1$ = yellow pixels, $\boldsymbol{K}_2$ = blue pixels, $\boldsymbol{K}_3$ = green pixels, and $\boldsymbol{K}_E$ = brown pixels. (c) Practical example.

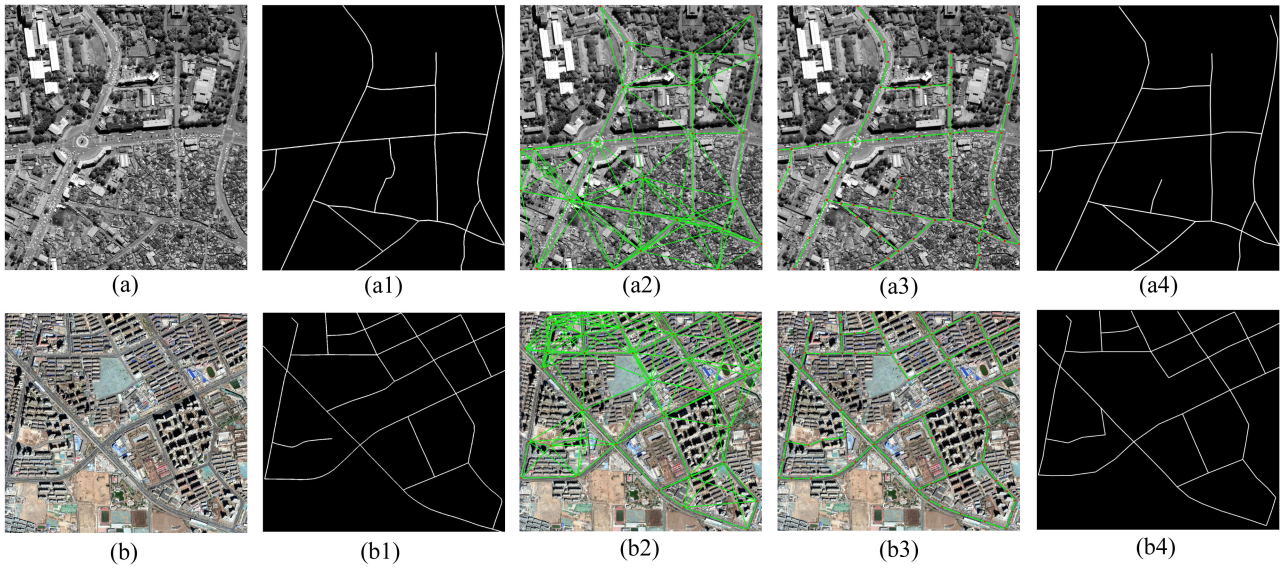

Fig. 13. (a) Worldview-1 image. (b) Google Earth image. (a1) and (b1) Reference lines. (a2) and (b2) Initial road networks [(a2): 26 points and 91 lines and (b2): 36 points and 134 lines].. (a3) and (b3) Final road networks [(a3): 66 points and 70 lines and (b3): 84 points and 92 lines]. (a4) and (b4) Separated results.

where ϕ is the function that computes the number of pixels, K_h is the cumulative sum of pixel percentages in h layers. Therefore, $K_0 = k_0$ represents accuracy of extraction and K_h ($h > 0$) represents extraction rate in the h layers of buffer region.

B. Results and Discussions

To illustrate the advantages of the proposed algorithm, the corresponding experimental results are showed and analyzed. First, Fig. 13 gives two experimental results obtained from the proposed algorithm. Fig. 13(a) and (b) are testing images from Worldview-1 satellite (size: 1151 × 1257 pixels) and Google Earth (size: 2494 × 2303 pixels), respectively. The urban road scenes in Fig. 13(a) and (b) include clear geometry noise (cars) and objects (e.g., buildings) whose spectra are similar to road. Fig. 13(a2) and (b2) shows the feature points and initial networks of road. The feature points which are selected by users according to the road ends, bends end crossroads form $\boldsymbol{V}^{(0)}$. The initial networks which are generated by connecting the feature points according to the maximum and minimum distances (see Table I) form $\boldsymbol{L}^{(0)}$ and they almost cover the whole roads in whole scenes. Simulated from the road extraction model in (9) with the designed RJMCMC algorithm, the final feature points and networks are showed in Fig. 13(a3) and (b3). It can be seen that all the feature points and networks are almost clustered in the road body rightly. Compared with the reference lines in Fig. 13(a1) and (b1), it can be seen that the road extraction results [see Fig. 13(a4) and (b4)] are continuous and smooth except the extremely unclear road segments. It illustrates that the proposed algorithm combining the geometry and network topology structure characteristics of road can avoid the interference of geometric noises and similar spectra. Moreover, Table III gives the evaluation results calculated according to the buffer evaluation method, the accuracy (K_0) and extraction rate (K_3) of extraction results can reach 61.35% and 98.99%, respectively. Therefore, the proposed algorithm for urban road extraction is practicable.

TABLE III
QUANTITATIVE EVALUATION OF BUFFER

Experiment result	Accuracy	Extraction rate			Simulation time (min)
	K_0 (%)	k_1 / K_1 (%)	k_2 / K_2 (%)	k_3 / K_3 (%)	
Fig. 13 (a4)	59.74	32.18 / 91.92	6.53 / 98.45	0.51 / 98.96	15.4573
Fig. 13 (b4)	61.35	31.44 / 92.79	6.12 / 97.91	1.08 / 98.99	25.6792
Fig. 14 (a2)	54.21	31.52 / 85.73	7.04 / 92.77	1.66 / 93.43	23.5384
Fig. 14 (b2)	60.17	32.73 / 92.90	5.33 / 98.23	0.68 / 98.91	10.3794
Fig. 16 (a2)	48.61	30.05 / 78.66	10.17 / 89.83	3.03 / 92.86	22.5693
Fig. 16 (a3)	59.23	29.69 / 88.92	7.58 / 96.50	1.48 / 97.98	3.2356
Fig. 16 (b2)	42.72	21.24 / 63.96	9.63 / 73.59	11.21 / 84.80	34.1743
Fig. 16 (b3)	53.82	26.18 / 80.01	5.28 / 85.29	2.23 / 87.52	12.9345

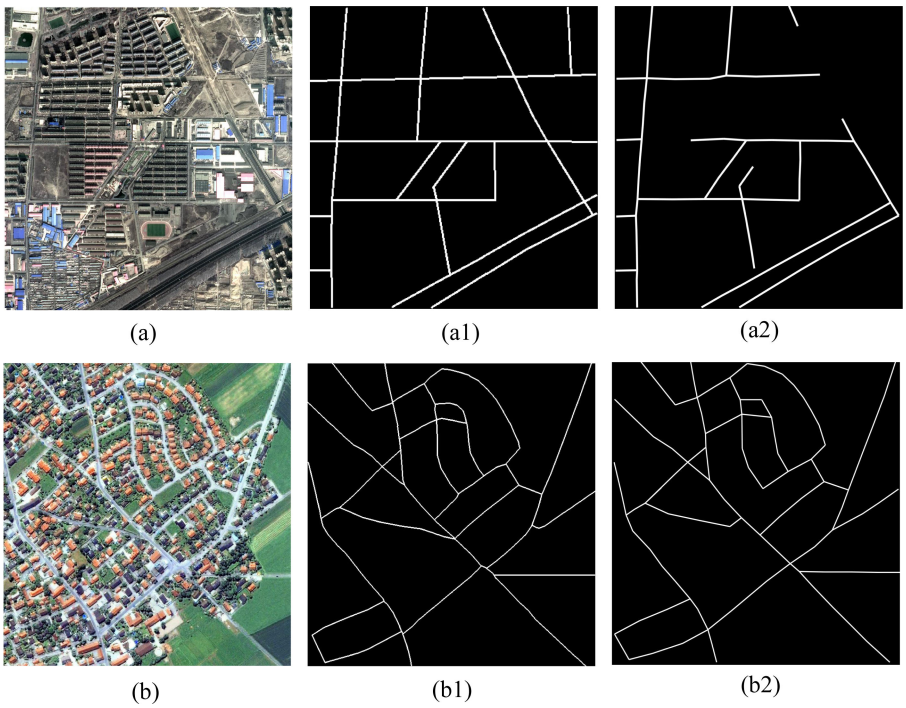

Fig. 14. (a) Gaofen-2 image with 2144 × 2226 pixels. (b) Ikonos image with 700 × 700 pixels. (a1) and (b1) Reference lines. (a2) and (b2) Results from the proposed algorithm [(a3): 66 points and 70 lines and (b3): 84 points and 92 lines].

Second, Fig. 14 shows the road extraction results from more complex road scenes. The testing images are Fig. 14(a) (size: 2144 × 2226 pixels) from Gaofen-2 satellite and Fig. 14(b) (size: 700 × 700 pixels) from Ikonos satellite. It can be seen that the spectral characteristic of road in Fig. 14(a) is weak, the structure of road in Fig. 14(b) is curved and complex. Although characteristics and sizes of two road scenes are great, the numbers of feature points (and initial lines) are controlled to be almost same. From the extraction results Fig. 14(a2) and (b2), it can be seen that both the extracted road networks are continuous and complete except the extremely unclear road parts. Moreover, as shown in Fig. 15, the convergence rates are similar within t = 9650 iterations. Besides, it can be seen in Table III that the accuracy and extraction rate of Fig. 14(a2) are up to 54% and 93%, and of Fig. 14(b2) are up to 60% and 98%, respectively. From Table III, the computation time is not raised when size of testing image is increased. Overall, it can be illustrated that the proposed algorithm can extract the road networks from urban road scenes with different sizes and characteristics effectively.

Finally, Fig. 16 gives the comparing results from the previous PP-based algorithms and the proposed algorithm. The testing images are Ikonos image (size: 400 × 400 pixels) and QuickBird image (size: 1024 × 1024 pixels). Fig. 16(a2) and (b2) are results from the algorithms proposed by [18] and [19], respectively. It can be seen in Fig. 16(a2) and (b2) that the results are not continuous at some crossroads (see the red boxes) or shaded roads (see the blue boxes). The comparing algorithms only model the connectivity between road segments and ignore connectivity between points and road segments. Moreover, the spectral characteristic of shaded roads is weak, so it is hard for the comparing algorithms to extract the shaded roads rightly. Comparatively, the proposed algorithm uses the CPP to model the feature points in road and define the freedom degree of points to constrain connectivity between points and road segments.

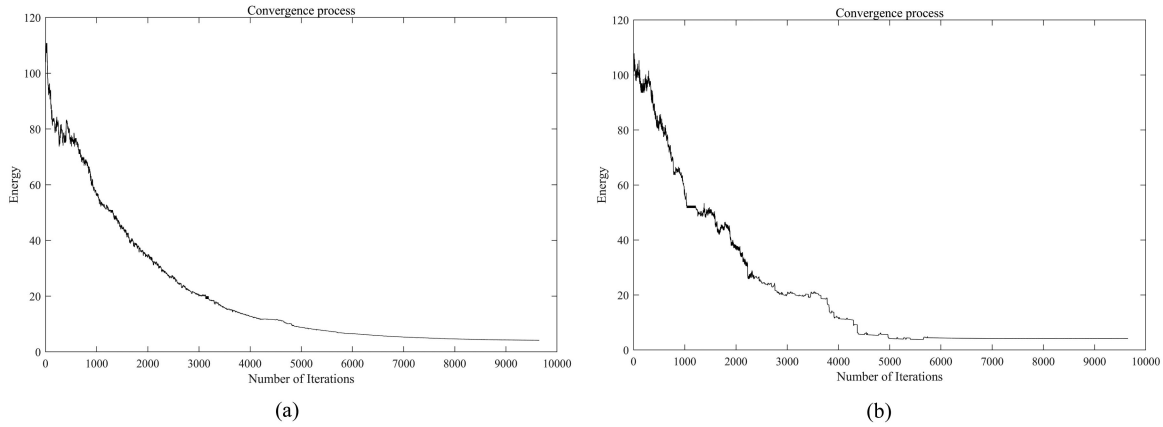

Fig. 15. Convergence process. (a) Convergence process of Fig. 14(a2). (b) Convergence process of Fig. 14(b2).

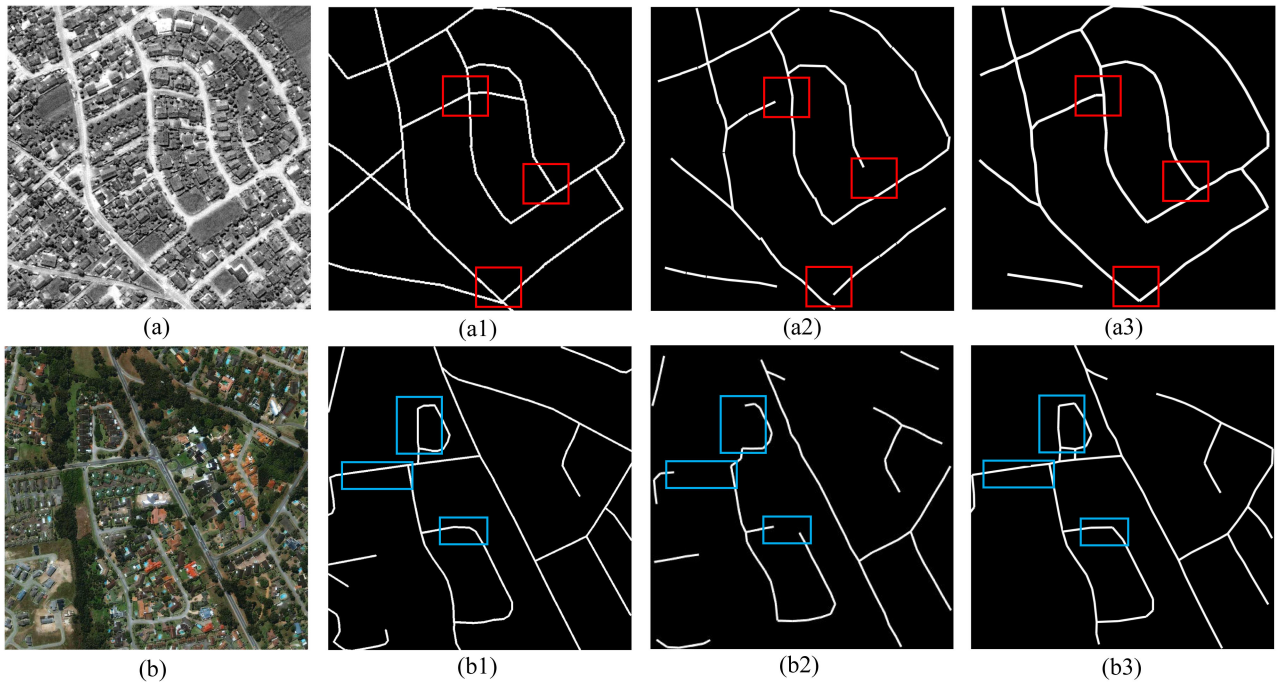

Fig. 16. (a) Ikonos image. (b) Quickbird image. (a1) and (b1) Reference lines. (a2) Result from the algorithm proposed by [18]. (b2) Result from the algorithm proposed by [19]. (a3) and (b3) Results from the proposed algorithm.

Therefore, as shown in Fig. 16(a3) and (b3), the road extraction results are more complete and continuous. Besides, Table III gives the accuracy, extraction rate and simulating time. It verifies that the proposed algorithm can extract the complex urban roads more accurately and completely than the PP-based algorithms. Moreover, the simulating time of PP-based algorithms is much longer than the proposed algorithm. Overall, it is illustrated that the proposed algorithm can extract the road system efficiently.

IV. Conclusion

This article presents the CPP-based network topology structure constrained urban road extraction algorithm. The CPP is used to model the feature points in the road system. Based on that, an initial network topology structure is constructed. The road extraction model constructed by constraining the network topology structure and the spectra of road can form a continuous network quickly. The RJMCMC algorithm with designed transfer operations, such as birth, death, move of points in CPP, and birth, death and transformations of lines in network topology structure can simulate from the road extraction model effectively. The proposed algorithm can be applied to different datasets and can effectively extract the continuous road networks in the complicated urban scenes. Moreover, compared with the results from the existing road extraction algorithms, it proves that the proposed algorithm can extract the higher quality road network from remote sensing images with complex spectral and structural characteristics. However, what is worth noting is that the proposed algorithm needs the feature points in advance, which reduces the full automation of algorithm. Therefore, the article for selecting the feature points automatically is necessary. Moreover, to construct an automatic and high-efficient road extraction algorithm, the top-down methodology designed from the network structures to geometrical structures and then to pixel points is worth studying.

REFERENCES

[1] M. Soilán *et al.*, "Automatic extraction of road features in urban environments using dense ALS data," *Int. J. Appl. Earth Observ. Geoinf.* vol. 64, pp. 226–236, Feb. 2018.

[2] Z. Gong, L. Xu, Z. Tian, J. Bao, and D. Ming, "Road network extraction and vectorization of remote sensing images based on deep learning," in *Proc. IEEE 5th Inf. Technol. Mechatronics Eng. Conf.*, 2020, pp. 303–307.

[3] F. Huang, Z. Liu, and T. Xie, "Road extraction from aerial image data via multiple features integrated with convolution long short time memory unit network," *Remote Sens. Lett.*, vol. 11, no. 11, pp. 1012–1021, Sep. 2020.

[4] S. P. Kearney *et al.*, "Maintaining accurate, current, rural road network data: An extraction and updating routine using Rapideye, participatory GIS and deep learning," *Int. J. Appl. Earth Observ. Geoinf.*, vol. 87, May 2020, Art. no. 102031.

[5] X. Song *et al.*, "A suitability evaluation of urban road network topology for conventional bus transits," *Urban Plann. Forum*, vol. 4, pp. 43–50, Jun. 2020.

[6] L. Li and Y. Liu, "A fast algorithm for road recognition in remote sensing image," *Adv. Mater. Res.*, vol. vol., no. 108–111, pp. 1344–1347, May 2010.

[7] Z. Wang, M. Zhang, and W. Liu, "An effective road extraction method from remote sensing images based on self-adaptive threshold function," in *Proc. Asia-Pac. Signal Inf. Process. Assoc. Annu. Summit Conf.*, 2019, pp. 455–460.

[8] W. Zhao *et al.*, "Road extraction in remote sensing images based on spectral and edge analysis," *Spectrosc. Spectral Anal.*, vol. 35, no. 10, pp. 2814–2819, Oct. 2015.

[9] W. Huang *et al.*, "An improved road extraction method for remote sensing images based on Canny edge detection," *Remote Sens. Land Resour.*, vol. 31, no. 1, pp. 65–70, Mar. 2019.

[10] P. Zdeněk, "Road tracking method suitable for both unstructured and structured roads," *Int. J. Adv. Robot. Syst.*, vol. 10, no. 3, pp. 1–10, Jan. 2013.

[11] J. Han *et al.*, "Road boundary detection and tracking for structured and unstructured roads using a 2D lidar sensor," *Int. J. Automot. Technol.*, vol. 15, no. 4, pp. 611–623, Jun. 2014.

[12] M. Li *et al.*, "Region-based urban road extraction from VHR satellite images using binary partition tree," *Int. J. Appl. Earth Observ. Geoinf.*, vol. 44, pp. 217–225, Feb. 2016.

[13] J. Zhang and X. Lin, "Semi-automatic extraction of straight roads from very high resolution remotely sensed imagery by a fusion method," *Sensor Lett.*, vol. 11, no. 6/7, pp. 1229–1235, Jun. 2013.

[14] K. Kumar, A. Velayudham, and R. Kanthavel, "An efficient method for road tracking from satellite images using hybrid multi-kernel partial least square analysis and particle filter," *J. Circuits Syst. Comput.*, vol. 26, no. 11, Apr. 2017, Art. no. 1750181.

[15] S. N. Chiu *et al.*, *Stochastic Geometry and Its Applications*. Hoboken, NJ, USA: Wiley, ch.2, 2013, pp. 35–56.

[16] C. Lacoste, X. Descombes, and J. Zerubia, "Point processes for unsupervised line network extraction in remote sensing," *IEEE Trans. Pattern Anal. Mach. Intell.*, vol. 27, no. 10, pp. 1568–1579, Oct. 2005.

[17] D. Chai, W. Förstner, and F. Lafarge, "Recovering line-networks in images by junction-point processes," in *Proc. IEEE IEEE Conf. Comput. Vis. Pattern Recognit.*, 2013, pp. 1894–1901.

[18] J. He and S. Zhong, "Road network extraction from remote sensing image based on modified marked point process," *Comput. Eng. Appl.*, vol. 49, no. 17, pp. 150–153, Apr. 2013.

[19] Q. Zhao *et al.*, "Road extraction from remote sensing image based on marked point process with local structure constraints," *Chin. J. Sci. Instrum.*, vol. 41, no. 7, pp. 185–195, Aug. 2020.

[20] V. Schmidt, *Stochastic Geometry, Spatial Statistics and Random Fields: Models and Algorithms*. Cham, Switzerland: Springer, ch. 2, 2015, pp. 31–49.

[21] J. Dongnian, L. Wei, and S. Fuyuan, "Incipient fault diagnosis and amplitude estimation based on K-L divergence with a Gaussian mixture model," *Rev. Sci. Instrum.*, vol. 91, no. 5, May 2020, Art. no. 055103.

[22] Y. Zhang *et al.*, "Robust fault-detection based on residual K-L divergence for wind turbines," *IET Renew. Power Gener.*, vol. 13, no. 13, pp. 2400–2408, Jul. 2019.

[23] D. Hartley and S. French, "A Bayesian method for calibration and aggregation of expert judgement," *Int. J. Approx. Reasoning*, vol. 130, no. 1, pp. 192–225, Mar. 2021.

[24] E. Altman *et al.*, "Stochastic geometric models for green networking," *IEEE Access*, vol. 3, pp. 2465–2474, Nov. 2015.

[25] A. Schmidt *et al.*, "Forest point processes for the automatic extraction of networks in raster data," *ISPRS J. Photogramm. Remote Sens.*, vol. 126, pp. 38–55, Apr. 2017.

[26] E. Barca *et al.*, "A new supervised classifier exploiting spectral-spatial information in the Bayesian framework," *Int. J. Appl. Earth Observ. Geoinf.*, vol. 86, Nov. 2019, Art. no. 101990.

[27] M. Maleki and R. B. Arellano-Valle, "Maximum A-Posteriori estimation of autoregressive processes based on finite mixtures of scale-mixtures of skew-normal distributions," *J. Statal Comput. Simul.*, vol. 87, no. 6, pp. 1061–1083, Oct. 2017.

[28] M. Pereyra, J. M. Bioucas-Dias, and M. A. T. Figueiredo, "Maximum-A-Posteriori estimation with unknown regularisation parameters," in *Proc. 23rd Eur. Signal Process. Conf.*, 2015, pp. 230–234.

[29] O. Karakus, E. E. Kuruoglu, and M. A. Altinkaya, "Beyond trans dimensional RJMCMC with a case study in impulsive data modeling," *Signal Process.*, vol. 153, pp. 396–410, Jan. 2018.

[30] D. W. Kim, C. Aguilar, H. Zhao, and M. L. Comer, "Narrow gap detection in microscope images using marked point process modeling," *IEEE Trans. Image Process.*, vol. 28, no. 10, pp. 5064–5076, Oct. 2019.

[31] T. Michels, D. Berh, and X. Jiang, "An RJMCMC-based method for tracking and resolving collisions of drosophila larvae," *IEEE/ACM Trans. Comput. Biol. Bioinf.*, vol. 16, no. 2, pp. 465–474, Mar./Apr. 2017.

[32] Y. Lin, X. Chen, and Y. Chen, "Fast flow calculation method with Jacobian matrix inverse preconditions," *Comput. Technol. Automat.*, vol. 38, no. 2, pp. 72–75, Jun. 2019.

[33] T. Ikeda *et al.*, "Aerial manipulator control method based on generalized Jacobian," *Res. Number Theory*, vol. 7, no. 2, pp. 231–241, Apr. 2021.

[34] Y. Li, J. Li, and Y. Lu, "A fuzzy segmentation based approach to extraction of coastlines from IKONOS imagery," *Geomatica*, vol. 62, no. 4, pp. 396–408, Jan. 2008.

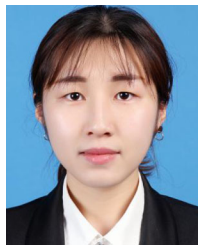

You Wu received the bachelor's degree from Liaoning Technical University, Fuxin, China, in 2017. She is currently working toward the Ph.D. degree with the School of Geomatics, Liaoning Technical University.

In 2017, she became a Postgraduate Student with Liaoning Technical University. In 2019, she successfully applied for the doctoral qualification without taking an entrance exam. Her main research interests include identification and extraction of remote sensing image information.

Quanhua Zhao received the M.Sc. and Ph.D. degrees in surveying and mapping from Liaoning Technical University, Fuxin, China, in 2004 and 2009, respectively.

She is currently a Professor and the Doctoral Supervisor with Liaoning Technical University. Her main research interests include modeling and analysis of remote sensing image, and application of random geometry.

Zhaoyu Shen is currently working toward the Postgraduate degree in surveying and mapping with the School of Geomatics, Liaoning Technical University, Fuxin, China.

His main research interests include identification of remote sensing image information.

Yu Li received the Ph.D. degree in surveying and mapping from the University of Waterloo, Waterloo, ON, Canada, in 2010.

He is currently a Professor and the Doctoral Supervisor with Liaoning Technical University, Fuxin, China. His main research interests include remote sensing data processing theory and basic application research, including spatial statistics, random geometry, fuzzy mathematics, object geometry, and feature extraction.